OBSERVATIONAL RESEARCH

Diurnal variability of atmospheric water vapour, precipitation and cloud top temperature across the global tropics derived from satellite observations and GNSS technique

Zofia Baldysz[1] · Grzegorz Nykiel[1,2] · Dariusz B. Baranowski[3] · Beata Latos[3] · Mariusz Figurski[1]

Abstract

The diurnal cycle of convection plays an important role in clouds and water vapour distribution across the global tropics. In this study, we utilize integrated moisture derived from the global navigation satellite system (GNSS), satellite precipitation estimates from TRMM and merged infrared dataset to investigate links between variability in tropospheric moisture, clouds development and precipitation at a diurnal time scale. Over 16 years of observations were analysed to estimate the diurnal cycles for 42 sites that span across the global tropics and assess the GNSS precipitable water vapour suitability in tropical moisture variability studies. Results show that the GNSS technique can be successfully used for studies related to the high-resolution temporal variability of integrated atmospheric moisture and, thus, in the analysis of multi-scale interactions and clouds development. For most of the analysed cases, GNSS integrated humidity shows one daily maximum (regardless of the season), which is related to the afternoon precipitation and cloud top temperature daily minimum. Although diurnal integrated moisture variations typically do not exceed 2 mm (usually below 5% of the daily mean value), in favourable large-scale conditions such relatively small changes can lead to the development of convective clouds and can affect precipitation distribution. Thus, GNSS technology allows reliable monitoring of tropospheric moisture variability at a diurnal time scale, which can be leveraged for improved monitoring and prediction of high-impact weather.

Keywords Humidity · Diurnal cycle · Atmospheric convection · Global tropics · PWV · GNSS

1 Introduction

The diurnal cycle is the primary mode of convective variability in the tropical environment (Janowiak et al. 1994; Dai et al. 2001; Chen and Houze 1997; Yang and Slingo 2001). Organized deep convection is responsible for the vertical distribution of clouds and water vapour across the tropics (Ciesielski et al. 2018). Thus, monitoring and understanding its diurnal features, including seasonal and regional differences, is important for a better understanding of weather variability in the tropics.

Diurnal characteristics of atmospheric convection, such as the horizontal and vertical extent of clouds and rainfall, differ significantly between land and ocean (Nesbitt and Zipser 2003; Baranowski et al. 2016, 2019). Depending on the underlying surface type, the diurnal cycle of the tropical deep convection may be assigned to the three main regimes: oceanic, continental and coastal (Kikuchi and Wang 2008). Typical features of the oceanic diurnal cycle are an early morning peak and moderate amplitude, while the continental one has an afternoon peak and a distinct amplitude. Such behaviour in the tropical diurnal cycle of precipitation was found in studies based on both in-situ measurements (Ray 1928; Gray and Jacobson 1977; McGarry and Reed 1978; Serra and McPhaden 2004) and satellite observations (Albright et al. 1985; Nesbitt and Zipser 2003; Tian et al. 2004; Yang et al. 2008). The coastal regime, in turn, displays a more complex nature, distinguishing features typical for seaside and landside regions (Kikuchi and Wang 2008). The

✉ Zofia Baldysz
zbaldysz@igf.edu.pl

1. Institute of Meteorology and Water Management, 01-673 Warsaw, Poland

2. Faculty of Civil and Environmental Engineering, Gdansk University of Technology, 80-233 Gdansk, Poland

3. Institute of Geophysics Polish Academy of Science, 01-452 Warsaw, Poland

seaside subregime is represented by large amplitude, off-shore phase propagation and peak that tends to occur from late evening to the next day noon. The landside subregime is similar in terms of amplitude, but in this case, a landward phase propagation is accompanied by a peak that occurs from noon to evening. Coastal diurnal evolution of precipitation can be found, for example, along the coasts of all major islands within the Maritime Continent (Baranowski et al. 2016; Hassim et al. 2016; Sakaeda et al. 2020; Marzuki et al. 2021). As presented by Kikuchi and Wang (2008), a division into seaside and landside subregimes can be successfully applied to many localizations across the global tropics. Several studies, however, have noted that the precipitation diurnal cycle may simply be characterized by a long weak nocturnal peak over open oceans and a relatively narrow and strong afternoon peak over lands (Ramage 1964; Wallance 1975; Gray and Jacobson 1977; Ruppert and Johnson 2015).

Depending on the underlying surface type, different mechanisms have been recognized to control the development and evolution of convective clouds. Over land, diurnal variability is mostly driven by solar heating of the surface and the planetary boundary layer: daytime insolation increases the lower-tropospheric temperature, and hence instability that leads to the water vapour uplifting, its condensation and, in consequence, afternoon rainfall. Night-time radiative cooling enhances stability and suppresses convection (Yang and Slingo 2001). Exceptions of this rule are low-level jet or orography forced convective scenarios in which rainfall may occur during the night-time (Bonner 1968). A less homogeneous mechanism occurs over the tropical ocean areas. In that case, the rainfall is often forced by organized, long-lived, deep convective systems (Gray and Jacobson 1977), of which intensification through the night is driven by differential radiative properties between cloudy and clear sky regions and results in early morning rainfall maximum (Nicholls 2015). Such mechanism has been identified in mesoscale convective systems, tropical cyclones, the intertropical convergence zone (ITCZ) and other large-scale convergence zones (Mapes and Houze 1993; Bowman and Fowler 2015; Ciesielski et al. 2018; Kikuchi and Wang 2008; Bain et al. 2010), which all show a robust, broad, early-morning precipitation peak. On the other hand, less intensive, diurnal solar heating of the sea surface may lead to shallow convection (Chen and Houze 1997; Bellenger et al. 2010; Rupert and Johnson 2016) and afternoon rainfalls over the open ocean. This canonical distinction is modulated by other environmental factors, such as large-scale conditions (e.g. seasonality) as well as local conditions (e.g. orography and/or sea-breeze circulation in the coastal zone) (Torri et al. 2019; Marzuki et al. 2021).

Tropical deep convection has been analysed using various techniques. Many studies have been based on satellite infrared (IR) data, especially in terms of analysis of diurnal variations in cloudiness and its characteristics (Yang and Slingo 2001; Smith and Rutan 2003; Wu and Ruan 2016; Chepfer et al. 2019). Such data have been used to estimate tropical precipitation as well. However, in such a case issues related to the conversion between IR radiance and rainfall must be considered (Tian et al. 2004). Many studies of a diurnal cycle of rainfall in the tropics have been based on data from the Tropical Rainfall Measuring Mission (TRMM) (Simpson et al. 1996) or later Global Precipitation Measurement (GPM) (Hou et al. 2014). Since their onboard precipitation radars measure reflectance from raindrops, obtained results are far less constrained by conversion formulas and thus widely used in tropical precipitation studies (Takayabu 2002; Nesbitt and Zipser 2003; Bowmann et al. 2005; Liu and Zipser 2008; Biasutti et al. 2012), albeit insufficient diurnal sampling at any given location.

Monitoring of atmospheric thermodynamic conditions has historically been a domain of soundings. However, apart from intensive observation periods, those are done daily or twice daily. As a result, the temporal resolution of soundings is too coarse to resolve diurnal variability. Additionally, in most cases such measurements require personnel (fully automated sounding stations are very rare), are expensive and suffer from balloon drift (Seidel et al. 2011).

Considering the limitations of traditional humidity measuring techniques, information about water vapour content can be obtained through so-called Global Navigation Satellite Systems (GNSS) meteorology (Bevis et al. 1994; Guerova et al. 2016; Jones et al. 2020). GNSS is an available, weather-independent, cost-effective, automated technique for continuous monitoring of integrated atmospheric moisture content (precipitable water vapour, PWV) with high temporal (even up to seconds) and spatial (hundreds of permanent stations) resolutions over all major land areas. Furthermore, GNSS equipment can be installed on vessels to leverage this technology for ocean measurements (Bosser et al. 2021). GNSS observations are highly sensitive to the changes in the integrated water vapour content in the atmosphere, and a mean bias between GNSS PWV and radiosonde PWV is around 1 mm (Barindelli et al. 2018; Ding et al. 2022). Therefore meteorological events that affect integrated moisture content, on various time scales, can be studied with this technique. For several decades, GNSS observations have been used for various meteorological applications (Vaquero-Martínez and Antón 2021) such as monitoring typhoons (Zhao et al. 2018) and severe weather events (Nykiel et al. 2019), predicting lightning (Suparta and Ali 2014) and heavy precipitation (Benevides et al. 2015), or studies on deep convection (Adams et al. 2013). GNSS PWV can also be a reliable input for storm nowcasting systems (Guerova et al. 2022). Because GNSS reference stations have been operating for about 30 years, those observations can also find applications in climate studies (Gradinarsky et al. 2002), that

leverage long time series for analyses of water vapour linear trends (Baldysz et al. 2018; Parracho et al. 2018) or water vapour interannual variability in response to climate modes such as El Niño–Southern Oscillation (ENSO) (Baldysz et al. 2021). GNSS has been used for water vapour diurnal cycle analysis as well. However, to date, they focused on regional networks rather than global applications. Analyses of the relationship between variability on a diurnal time scale of GNSS-derived moisture and other meteorological state variables over parts of South America (Meza et al. 2020; Serrano-Vincenti et al. 2022), Sumatra (Torri et al. 2019), Spain (Ortiz et al. 2011) and Japan (Li et al. 2008) can be mentioned here. Nevertheless, a detailed, comprehensive analysis of the relationship between GNSS PWV and precipitation across the global tropics is still lacking.

This paper documents that properly processed GNSS observations can be used to better elucidate the coupling between moisture variability and precipitation on a diurnal time scale within the global tropics. In the next section, we describe GNSS measurements, as well as brightness temperature, and precipitation data used in this study. Section 3 contains the methodology of GNSS PWV estimation and the approach to diurnal variability determination. In Results (Sect. 4), we focused on metrics of the diurnal variations in various environments, their mean values across global tropics, and divergent diurnal behaviour between GNSS PWV, cloud top height, and precipitation. We also take a closer look at diurnal cycle characteristics during different seasons. Finally, we present conclusions and discussions.

2 Data

The study utilises multiple sources of remote sensing data, which provide information on the variability of the atmospheric properties with temporal resolution sufficient for an analysis of the diurnal cycle. Properties of interest include vertically integrated water vapour, cloud top temperature and precipitation rate. The GNSS observations obtained from the International GNSS Service (IGS) network were used to estimate variability in atmospheric water vapour content. Precipitation estimates are based on the data from Tropical Rainfall Measurement Mission (TRMM) and Global Precipitation Measurement (GPM) missions, while spatiotemporal variability in cloud top temperature was assessed based on the satellite-based merged infrared (IR) dataset.

2.1 GNSS

The quality-assured data from the IGS were used to estimate the diurnal evolution of the atmospheric water vapour. The 42 out of 500 permanent stations, which currently form the IGS network, were selected for this study. The selection was based on two criteria: the station's location and the length of the available time series. Since this study focuses on the global tropics, only stations located between 30° N and 30° S were considered. Each station has to be operational for at least 16 years but has to start collecting information no earlier than 2001 (which is the beginning of the period for which more precise GNSS orbit parameters that affect GNSS processing are available). Such a period allows sufficient statistics for calculating the diurnal cycle in the atmospheric water vapour and its seasonal variability, and on the other hand, it does not significantly reduce the number of GNSS stations (as in the case of a more extended reference period).

Fig. 1 Spatial distribution of the analysed GNSS stations (scale is logarithmic)
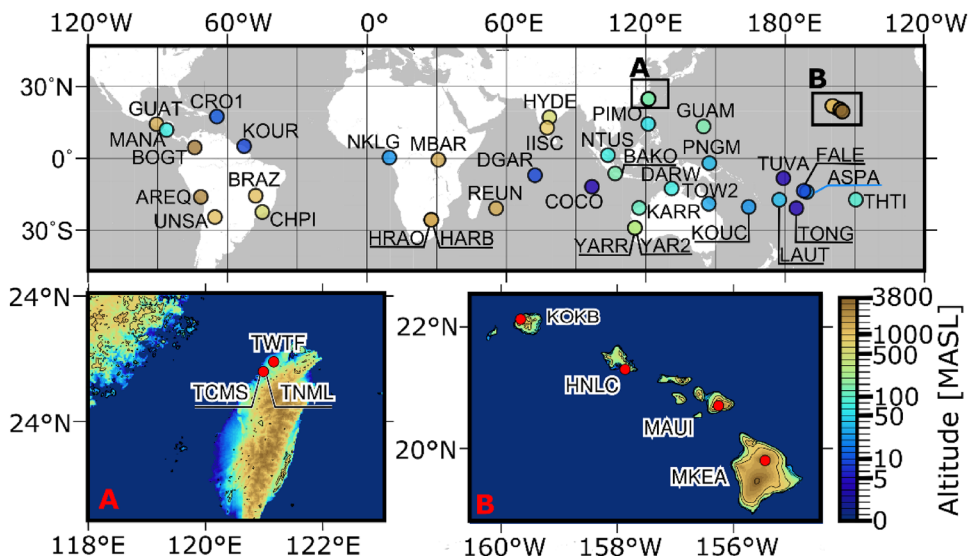
The spatial distribution of the selected stations is provided in Fig. 1, while detailed information about their localisation time span and data completeness is given in Table 2 (in the Appendix).

GNSS stations utilised in this study span all continents and are diverse in their elevation and distance from the coast. This provides an opportunity to investigate differences in the evolution of atmospheric water vapour in various environments. Thus, an opportunity for an analysis of diurnal coupling between moisture and precipitation goes beyond the regional domain (Li et al. 2008; Torri et al. 2019; Meza et al. 2020; Serrano-Vincenti et al. 2022). Most coastal stations are located below 100 m above sea level (ASL), except for some stations in the archipelagos of Hawaii and La Reunion. In particular, stations located on small islands of the Indian and Pacific Oceans, away from continents and big islands, are located at low elevations. On the other hand, in-land stations are scattered across various heights. Over half of them are positioned above 500 m ASL, which will strongly affect integrated water vapour content estimate and combined with local topography, influence its variability. Particular attention should be paid to the Hawaii archipelago, where 4 GNSS stations are located. Despite their proximity, they span over 3500 m in elevation range. Combined with complex topography, it will affect the estimated variability of the atmospheric water vapour.

Each station provides measurements of the time needed by a radio signal to travel to a ground receiver from all GNSS satellites in its field of view. The extra time required for the signal to propagate in the neutral atmosphere is expressed as the total path delay in the zenith direction above the receiver, known as the zenith total delay (ZTD). Each ZTD is constructed from all delays along a path between the ground receiver and all available GNSS satellites within a defined period. In this study, 30-s epochs were used, and calculations were performed with Bernese GNSS Software 5.2 (Dach et al. 2015). To perform calculations for each of the 42 ground stations independently, a precise point positioning (PPP) method was used. This method uses data from a single station to calculate ZTD at that location, thus reflecting changeable troposphere influence on the GNSS signal propagation only within this particular receiver and observed by this receiver satellites [about a 100 km radius around the station (Vaquero-Martínez and Antón 2021)]. Therefore, it prevents error propagation between stations. All ground station—GNSS satellite signals with elevation angles below 5° were excluded from the processing to reduce the multipath effect. The a priori troposphere, as well as tropospheric mapping functions (Herring 1992), were modelled using Vienna Mapping Functions 1 (VMF1) (Boehm et al. 2006). Precise ephemeris (orbits and clocks), which are of great importance for the PPP method's solution accuracy, were sourced from the second Center for Orbit Determination in Europe (CODE) reprocessing (Steigenberger et al. 2016). Both individual and type mean GNSS antenna calibrations were adopted. This approach enabled to obtain ZTD time series at each location. Finally, the time series were averaged to represent 1-hourly temporal resolution. As a result, for each station, a time series was at least 16 years long, had a temporal resolution of 1 h and was constructed solely based on inputs from a given station (e.g. no data from neighbour stations were used). Each time series was used to estimate integrated water vapour amount in the form of precipitable water vapour.

2.2 Precipitation

The Tropical Rainfall Measurement Mission gridded dataset (TRMM 3B42 v7) provides estimates of surface precipitation rate since 1998 with relatively high spatial (~0.25°) and temporal (3-hourly) resolutions (Huffman et al. 2010). Although the TRMM mission concluded in 2015, the TRMM 3B42 v7 production continued using data Global Precipitation Measurement mission, which replaced TRMM measurements. Gridded data were interpolated to each location of the 42 ground GNSS stations. Therefore, data representing 18 years between 01.2001 and 12.2018 (the maximum GNSS observations time span) with 3-hourly temporal resolution were used in this analysis. All precipitation data in this study come from the TRMM 3B42 v7 product (hereafter TRMM).

2.3 Cloud top temperature

Global, merged infrared (IR) dataset (Janowiak et al. 2001) provides estimates of cloud top temperature (brightness temperature—Tb) at 4 km spatial and 30-min temporal resolution based on data from geostationary satellites fleet. A gridded, multi-satellite product (Level 3) was used to assess temporal variability in a cloud population, represented by the evolution of a cloud top temperature, at each of the 42 ground GNSS stations. Similarly to the precipitation data, Tb data were interpolated to each location of the GNSS stations. Hence, at each point a Tb time series represents a local high frequency variability in cloud top temperatures. Therefore, Tb data characterize a diurnal evolution of a cloud field directly above each analysed location, which is comparable with the GNSS water vapour retrievals that are also expressed in the zenith direction. A cloud population in the tropics is dominated by convective clouds (Johnson et al. 1999). Therefore, observed evolution in cloud top temperatures on a diurnal time scale can be linked to cloud field variability, through an inferred relationship between the stage of atmospheric convection development and its vertical extent. Specifically, a development of a cloud field dominated by

convective clouds (e.g. from shallow to deep convection) will manifest itself in a decrease in cloud top temperatures, which can be measured with Tb data. It should be noted, that deep convective clouds in the tropics are often associated with upper-level clouds that can manifest with cold cloud tops resembling deep convective clouds. However, diurnal cycles of deep convective clouds and upper-level cloud types typically differ (Chepfer et al 2019). Therefore, a distinction based on their differentiated diurnal characteristics can be made between them. Deep convective clouds should show rapid changes in measured cloud top temperature and tend to occur in the afternoon, while larger-area anvil clouds show gradual changes in cloud top temperature and most frequently occur during evening and night (Chen and Houze 1997). Thus, cloud top temperature in this study primarily refers to the strength of atmospheric convection, measured by the vertical extent of convective clouds, identified based on infrared brightness temperature. Tb data for the period 01.2001–12.2018 (the GNSS collected observations time span) with 30 min temporal resolution were used in this analysis.

3 Methodology

3.1 Precipitable water vapour estimation based on GNSS data

A value of ZTD describes the total influence of the troposphere on GNSS radio signal propagation. It consists of delays caused by the hydrostatic (zenith hydrostatic delay—ZHD) and wet (zenith wet delay—ZWD) components. While ZHD depends on meteorological parameters such as pressure and temperature, the ZWD is related to water vapour content in the atmosphere. The ZTD, which is a direct product of GNSS observation processing, consists of an a priori ZHD value and its correction. This correction is often equated with ZWD, but it consists of both ZWD and correction to the incorrectly modelled ZHD. Therefore, in GNSS meteorology, the ZHD is also estimated a posteriori. This can be done through the Saastamoinen formula (Saastamoinen 1972) via meteorological parameters sourced from in situ measurements or meteorological reanalysis. In the next step, the ZHD is subtracted from ZTD to estimate ZWD, which reflects only the impact of the wet part of the atmosphere. The dependence of ZWD value on air humidity allows estimating the integrated property of the atmospheric water vapour content: an integrated water vapour (IWV), through the following formula (Bevis et al. 1992):

$$IWV = \Pi(T_m) \times ZWD, \tag{1}$$

where $\Pi(T_m)$ is a dimensionless quantity that can be obtain from the water vapour weighted mean temperature (T_m):

$$\Pi^{-1} = 10^{-8}(R_v \times (K_3 T_m + K_2')) \tag{2}$$

where R_v is the specific gas constant of water vapour and amounts to 461.5 [J/(kg K)], while K_2 and K_3 are the air refractivity parameters. In our study, the T_m value, was calculated using proposed by Bevis et al. (1992) linear relationship to the surface temperature sourced from the ERA5 ($T_m = 0.72 \cdot T_s + 70.2$). Information about water vapour content in the troposphere provided by IWV (unit: kg/m^2) can also be expressed via PWV parameter, by adjusting IWV by water vapour density (unit: mm). In this study, meteorological parameters (surface temperature and pressure) for each of 42 ground GNSS stations were sourced from surface level of ERA5 reanalysis (Hersbach et al. 2020) using bilinear interpolation (Kirkland 2010), while values of air refractivity index were taken from Rüger (2002).

All derived hourly PWV data from all stations for the investigated period are available as a netCDF file (Nykiel et al. 2023) for cross-validation and further analyses.

3.2 Diurnal cycle calculation

The diurnal cycle decomposition has been performed on all (PWV, precipitation, Tb) time series data at each location independently. We considered only the daily mean, diurnal and semi-diurnal harmonics which should reflect general changes during the day (Baranowski et al. 2019). First, the composite diurnal cycle has been calculated by averaging data over a specific period. Three such composites are used in this study: a monthly composite, a multi-year annual average and a multi-year seasonal average for each of the four seasons. For each of those composites, the averaged diurnal cycle has been calculated by averaging all available data at a given interval: hourly values for PWV, native 3-hourly values for precipitation and native 30-min values for Tb were used. Then, decomposition was performed by fitting the following function to composite such diurnal cycle data:

$$\begin{aligned} x(t) = \ & x_0 + A_A^I \times \sin(2\pi t) + A_A^O \times \cos(2\pi t) \\ & + A_{SA}^I \times \sin(4\pi t) + A_{SA}^O \times \cos(4\pi t) \end{aligned} \tag{3}$$

where, $x(t)$ denote for the composite diurnal cycle (24 h) time series based observed data and A_A^I, A_A^O, A_{SA}^I and A_{SA}^O are coefficients for the sine and cosine conditions using least square estimation method.

4 Results

The decomposition of the diurnal evolution of PWV, Tb and precipitation into the diurnal and semi-diurnal cycle is performed independently for each variable at all locations to investigate variability in a range of tropical climates. To show the performance of diurnal decomposition metrics and highlight key features associated with diurnal cycle in various environments, we begin with a detailed analysis of several sample stations based on a monthly averaged diurnal cycle, followed by mean diurnal cycle characteristics across all stations and seasonal variability of the diurnal decomposition. It should be noted that all analysis presented here are based on composites and highlight a typical, average diurnal evolution of PWV, Tb and precipitation.

4.1 Diurnal cycle metrics in various environments

An example of diurnal cycle decomposition on a subset of 6 stations is presented in Fig. 2. Selected locations represent various tropical environments, such as small islands and landlocked stations, various elevations and diurnal characteristics of investigated properties. The composite diurnal cycle of PWV (blue), Tb (purple), and precipitation (green) has been calculated based on monthly averaged data for either March or September 2016. The month's selection was arbitrary and presents an example of a 'wet' month at each location. This analysis shows the decomposition of diurnal evolution into diurnal and semi-diurnal modes and highlights differences in diurnal cycle properties between locations during an example of a wet month. It can be seen that decomposition (lines) follows the data (dots) and depicts the diurnal evolution of atmospheric humidity and Tb. The same is valid for precipitation (not shown). The range of the root mean square error for PWV decomposition is between 0.32 mm (LAUT/MBAR) and 0.47 mm (BAKO), while for Tb decomposition is between 1.44 K (FALE) and 2.51 K (PIMO). Thus, decomposition of composite diurnal cycle data into 24-h and 12-h modes realistically represents diurnal variations and will be applied throughout the rest of the study.

Stations BRAZ (Brasilia, Brazil, 1106.0 m ASL) and MBAR (Mbarara City, Uganda, 1337.7 m ASL) (Fig. 2a, b) are considered in-land, continental stations as they were located away from any coast. They are also characterised by high elevations, which is reflected in the relatively low mean PWV values. Selected months represent example rainy periods (Salgado et al. 2019; BakamaNume 2010). Stations BAKO (Cibinong, Indonesia, Java, 157.2 m ASL) and PIMO (Quezon City, Philippines, Luzon, 95.5 m ASL) are located on big islands of the Maritime Continent (Fig. 2c, d), while FALE (Faleolo International Airport, Samoa, Upolu Island,

47.6 m ASL) and LAUT (Lautoka, Fiji Island, 89.7 m ASL) stations are located on small islands (Fig. 2e, f) in the Pacific. All stations are in a tropical climate.

All stations show a clear variation of atmospheric water vapour content, cloud top temperature and precipitation at a diurnal time scale. However, differences between stations are apparent in the magnitude of a diurnal harmonic and the existence of a significant semi-diurnal cycle, exemplified by a second peak in a diurnal time series. Integrated water vapour contents show a single diurnal maximum at all presented stations. Diurnal variation in PWV is small (2–5 mm) in comparison to the daily mean value (30–60 mm), but a single maximum always occurs during the local afternoon (between 15 and 18 local time, LT), and a single minimum is observed between 3 and 9 LT. At BRAZ, MBAR and BAKO stations (that is continental and one of large islands' stations) maximum PWV is observed during the enhanced precipitation period, about 3 h after its peak value. At the PIMO station, maximum PWV occurs during maximum precipitation, but its decay afterwards is slower than at any other station. Although the scatter of PWV observations during the local afternoon is large at PIMO compared to other locations, its diurnal evolution is robust. At small island stations, PWV maximum occurs in sync with precipitation maximum and cloud top temperature minimum (LAUT) or about 3 h before (FALE).

The diurnal evolution of precipitation shows significant rainfall during the local afternoon, with maximum occurring between 13 and 19 LT at all locations. The largest diurnal maximum precipitation rate, exceeding 32 mm/day, is observed in BAKO station, while the smallest, slightly above 7 mm/day, is in FALE. A single mode distribution of precipitation characterizes continental stations (Fig. 2a, b) and large islands stations.

At PIMO station (Fig. 2d) precipitation shows a secondary afternoon maximum at 22 LT, which is associated with an downtick in cloud top temperatures (note that a Tb scale is inversed and see hourly averages, the feature is not picked up by the fitted diurnal cycle) and gradual decrease in PWV. Therefore, it appears to be related to secondary convection which can be driven by local dynamics such as shallow overturning breeze circulation (precipitation aligned with short-term decrease in Tb), as PIMO is a coastal station, and unrelated to local thermodynamic forcing as PWV is gradually decreasing.

Small islands' stations (FALE and LAUT) show a secondary, early morning peak at around 6 am. However, this early morning maximum is lower than the afternoon peak. At both locations it is associated with a larger than usual variability in cloud top temperature averages (dots) which translates into a slight decrease in decomposed data (lines). Such diurnal precipitation evolution over small islands can be related to the early morning peak in convective activity
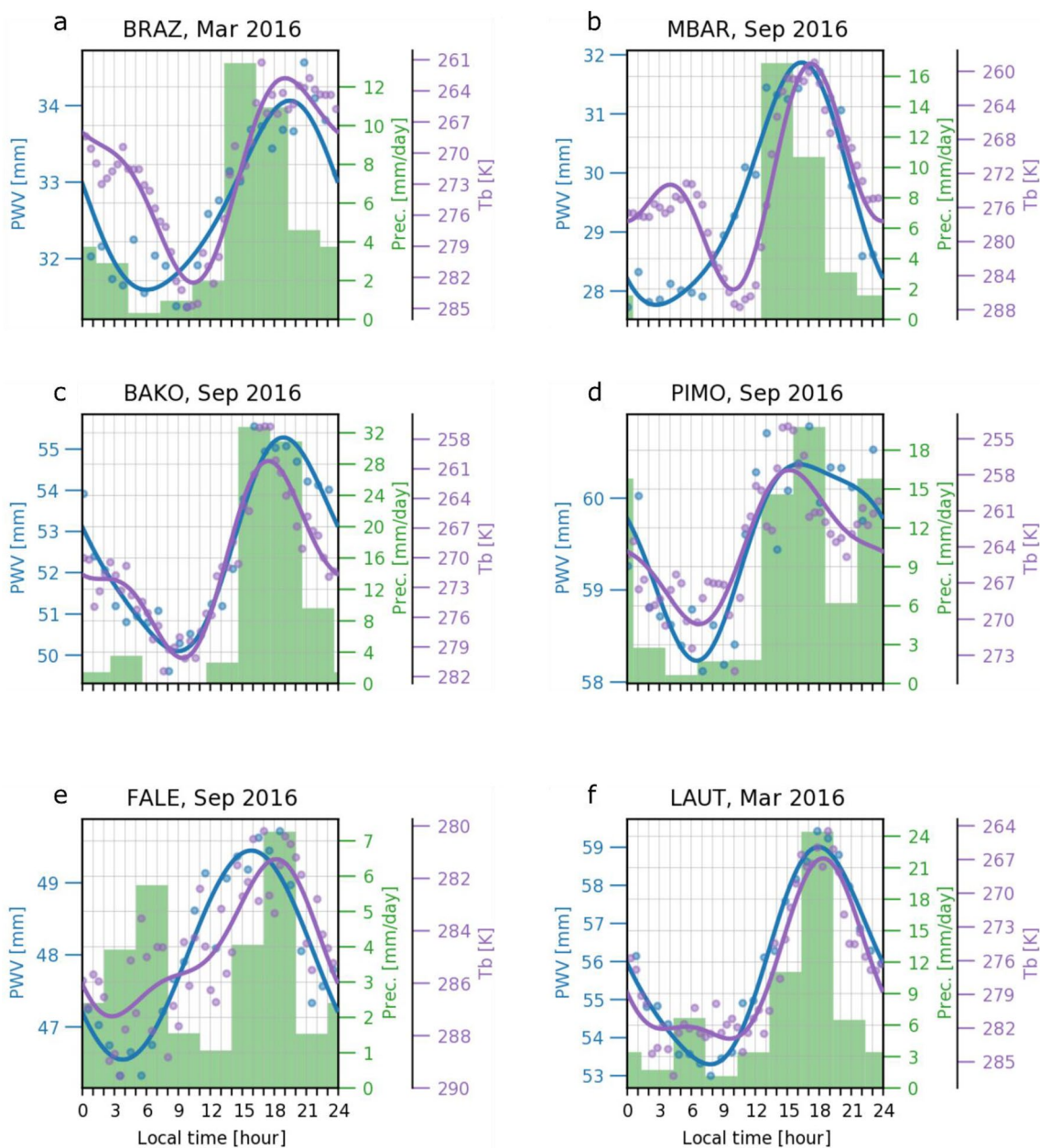
Fig. 2 Diurnal evolution of atmospheric properties averaged over a specific month. Shown are PWV (blue dots) and Tb of the clouds (purple dots) with fitted diurnal and semidiurnal decomposition curve (blue and purple line for PWV and Tb, respectively) and precipita- tions (green bar), for BRAZ (**a**), MBAR (**b**), BAKO (**c**), PIMO (**d**), FALE (**e**) and LAUT (**f**) stations for a selected month in 2016. Note that scales differ between panels

over surrounding oceans (Chen and Houze 1997; Dai 2001) driven by the interaction between radiative heating and clouds (Gray and Jacobson 1977). Therefore, unlike the afternoon precipitation maximum, it is not directly related to atmospheric moisture content, as exemplified by the diurnal PWV minimum at that time.

Cloud top temperature shows clear diurnal evolution as well. The minimum Tb (note that Tb axis in Fig. 2 is reversed) is observed during the local afternoon, a timing

in agreement with integrated water vapour and precipitation maxima. At most stations, the Tb minimum occurs in sync with PWV and about 3 h after precipitation maximum. Exceptions are PIMO station, where both Tb and PWV extrema occur before maximum precipitation and FALE station, where minimum cloud top temperature occurs in sync with maximum precipitation and 3 h after PWV maximum. Interestingly, all but PIMO stations show some semidiurnal variability in Tb, represented by a second minimum

in a diurnal evolution. The most pronounced semi-diurnal extremum in cloud top temperature is observed at MBAR station with a minimum at 4 LT, during diurnal precipitation and PWV minima. Semi-diurnal Tb signal can be observed at FALE and LAUT stations, in phase with early morning maximum precipitation and near the minimum in diurnal PWV evolution. These early morning Tb variations show cloud top temperature higher than during the daily afternoon minimum, indicating that nocturnal precipitation peak is associated with shallower cloud population in comparison with afternoon peak. At FALE station Tb points are scattered during the morning minimum, indicating substantial variability in cloud populations. However, overall diurnal evolution is small compared to other stations (in agreement with small PWV evolution) and the lowest early morning value is 283.5 K, which is higher than the typical value of 281.5 K during the daily minimum.

The above analysis of the six stations confirms that applied methods adequately represent the diurnal evolution of atmospheric properties, including diurnal and semi-diurnal evolutions. The primary feature at all stations is the daily maximum of integrated water vapour and precipitation, and minimum in cloud top temperature in the local afternoon. Furthermore, PWV shows clear mono–modal diurnal evolution with one daily maximum in the afternoon and one daily minimum early in the morning. At continental and large island stations, precipitation evolution and cloud top temperature (except MBAR station) show similar diurnal evolution. On the other hand, small islands' stations show a secondary peak in precipitation associated with a secondary minimum in cloud top temperature. The latter occurs near the daily minimum of the integrated water vapour, which indicates that precipitation is due to either cloud-radiation interaction processes typical for adjacent open ocean or relatively shallow clouds that can develop during sea-breeze-induced convergence over coast (Kousky 1980). These features are robust. However, caution should be used when analysing small differences in diurnal phases between variables because of the temporal resolution of datasets used and scatter among data points due to averaging.

4.2 The mean diurnal cycle across global tropics

Combined characteristics of diurnal evolution of atmospheric properties are shown in Fig. 3 in the form of a diagram, where the colour of a marker indicates the daily mean value, while the arrow shows an amplitude (length) and a phase (angle) of a leading mode (diurnal or semi-diurnal). The shape of markers indicates which mode has higher amplitude: circles are used when the diurnal amplitude is higher, while triangles are used when semi diurnal amplitude is larger. The mean diurnal cycle characteristics have been derived based on composite diurnal evolution, calculated at each station in the form of multi-year average diurnal cycle of precipitation, Tb and PWV.

The daily mean PWV ranges from 3.64 to 57.52 mm. Low values are generally associated with a high altitude of a station. Five of the smallest daily mean PWV values are found in mountainous environments of MKEA (Mauna Kea, Hawaii Island, 3754 m ASL), MAUI (Haleakala, Maui island, 3062 m ASL), AREQ (Peru, Arequipa, 2488 m ASL), REUN (Le Tampon, Reunion Island, 1558 m ASL) and KOKB (Waimea, Kauai Island, 1167 m ASL) stations, with mean values of 3.64 mm, 4.51 mm, 13.18 mm, 14.93 mm and 16.17 mm, respectively. In contrast, the highest values are found mostly on small islands and coastal areas of the Maritime Continent and Western Pacific. The daily averaged PWV exceeds 50 mm at stations such as PNGM (Lombrum, New Guinea—57.52 mm), NTUS (Singapore—52.85 mm), TUVA (Tuvalu—52.36 mm) and PIMO (Philippines, Quezon City—50.53 mm), NKLG (Gabon, Libreville—52.8 mm). Amplitudes of diurnal PWV variations are small compared to daily mean values and range between 0.13 mm (GUAM) and 2.47 mm (BAKO, Indonesia, Cibinong). A semi-diurnal PWV amplitude exceeds the diurnal one at only one location (MKEA). However, that station shows the lowest daily mean and the lowest diurnal amplitude across all 42 stations. Thus, we conclude that PWV across tropics shows mono-modal distribution with a single diurnal maximum. 32 stations (> 70%) show an amplitude of the diurnal mode higher than 0.5 mm with the maximum occurring during the local afternoon (3 pm–8 pm). Continental and large island stations show larger diurnal amplitude of PWV than small islands. Small islands in the south-west Pacific show large variability in the diurnal PWV amplitude, likely related to the variability within the South Pacific Convergence Zone (Matthews 2012). The difference between the magnitude of diurnal PWV variation between large and small islands indicates that a horizontal gradient from land's interior towards the coast can be expected (Torri et al. 2019). However, the spatial distance between stations analysed here is insufficient to fully analyse this variability and potential coupling with breeze circulation.

An overall good agreement between daily mean values of PWV and precipitation has been found. As expected, high integrated atmospheric moisture values are associated with high precipitation rates (e.g. BAKO), and low PWV values correspond to small precipitation values (e.g. AREQ). However, on a subdiurnal time scale, larger differences arise. In contrast to primarily mono-modal diurnal PWV evolution, 30% of stations are characterised by a semi-diurnal precipitation amplitude exceeding a diurnal one. The diurnal amplitude is high over continental and large island stations, where precipitation peaks in the local afternoon. The largest values of diurnal amplitude are found in South America, equatorial Africa and the Maritime Continent. An exception is KOUR

Fig. 3 Diurnal amplitude, phase and mean value of PWV (**a**), precipitation (**b**) and TB (**c**) estimated based on the all available time span. The length of the arrow represents amplitude value, direction of the arrow indicates phase expressed in local time (LT) and colour of the dot denotes mean value. Circles represent stations for which dominant amplitude was found for diurnal signal, triangles represent stations for which dominant amplitude was found for semidiurnal signal, while squares represent stations for which neither diurnal nor a semidiurnal amplitude was significant
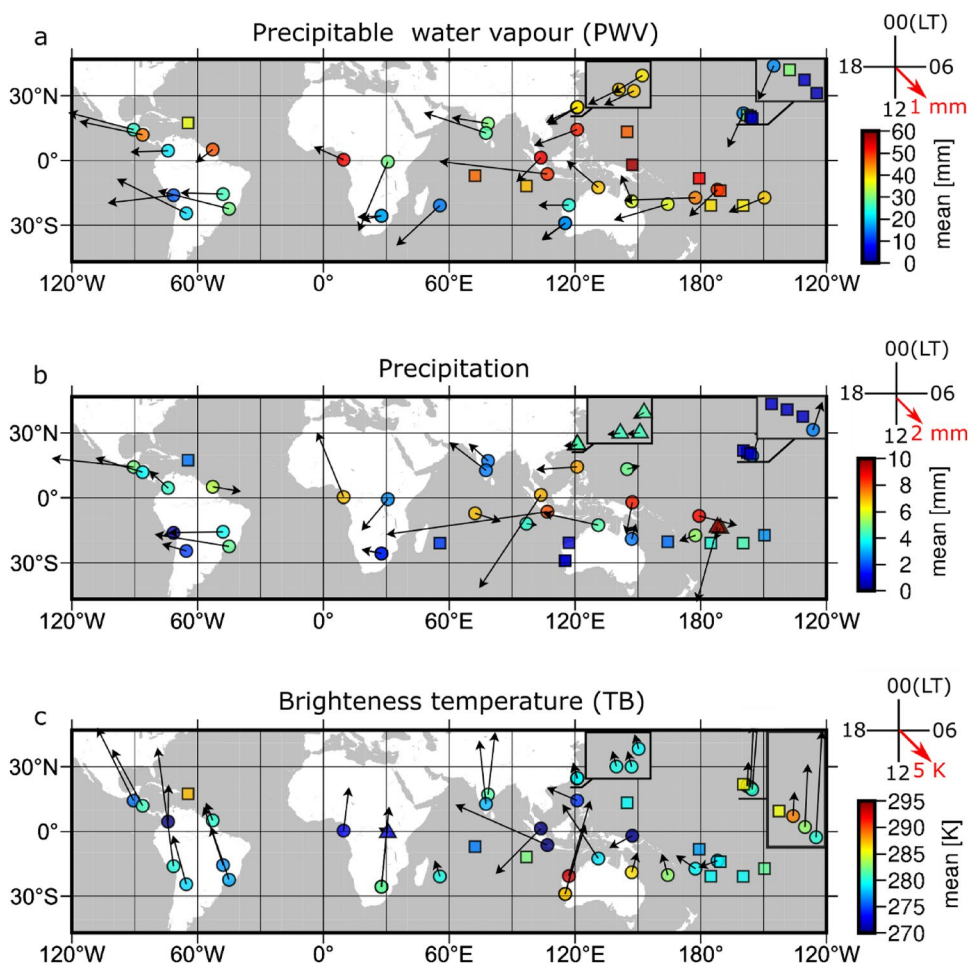
station in French Guiana with a peak of diurnal precipitation in the early morning (see Sect. 4.3). The semi-diurnal cycle is the primarily subdiurnal mode at small islands that show an overall small diurnal variation.

There are three stations (twin stations YARR and YAR2, and KARR) in western Australia, which show diurnal variability in PWV data, but no diurnal precipitation cycle. However, both stations are located in the semi-arid region, dominated by the subsiding branch of Walker circulation, where mean atmospheric water vapour content and precipitation are low. The substantial diurnal variability in PWV in that region, likely driven by a land-sea breeze circulation, is not sufficient to destabilize the atmosphere and create an environment favourable for convection and precipitation development.

On average, the maximum diurnal precipitation occurs in phase with a diurnal maximum in PWV (Fig. 4a, note that phase difference is shown for station with substantial diurnal amplitude). Most stations show phase differences in the range of ±2 h, which is smaller than the temporal resolution of precipitation data. An absolute mean phase difference between PWV and precipitation was 1h47m. One outlier

from this range was observed. At KOUR (French Guiana) station peak precipitation occurred nearly 9 h before peak PWV. PWV and precipitation phase difference exceeding a typical range has also been found at KARR (Australia) and THTI (French Polynesia) stations. At these stations, maximum precipitation occurred 3–3.5 h after PWV peak. However, this difference still indicates that peak precipitation and maximum integrated atmospheric moisture occur during local afternoon. Thus, diurnal PWV variations are related to afternoon precipitation maximum.

There are three primary features of diurnal cycle of cloud top temperature: the evolution is dominated by diurnal cycle, substantially larger diurnal variation over continental and large islands than small islands and shift in the phase towards later hours in comparison with diurnal peak in either PWV or precipitation. Minimum cloud top temperature consistently follows PWV maximum by several hours (Fig. 4b). The mean difference was 5h8m. Relatively the smallest phase shift is observed in the Maritime Continent region, e.g. at NTUS station (Singapore) minimum cloud top temperature occurs in phase with daily maximum PWV value. The largest lag of minimum cloud top temperature relative

Fig. 4 Differences in diurnal phase expressed in hours between Precipitable Water Vapour (PWV) and precipitation (**a**) and PWV and brightness temperature (TB; **b**) data. To ensure the reliability and minimize random sampling, the analysis was only performed at stations for which PWV leading amplitude was equal to or higher than 0.5 mm
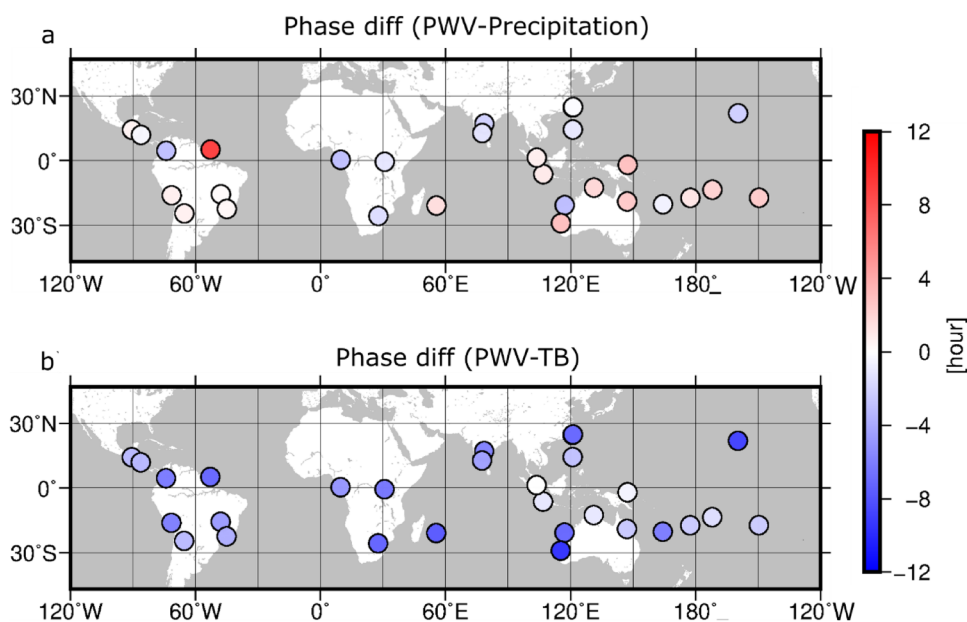

to maximum PWV has been observed at YAR2, YARR and KOKB stations and amounted to 9h32min, 9h26min and 8h55min, respectively.

This analysis shows that across global tropics a typical afternoon peak in precipitation is associated with diurnal minimum in cloud top temperature driven by increased tropospheric moisture content. This is consistent with coupling between radiation and turbulent fluxes on diurnal time scale, that trigger convection in conditionally unstable environment. In such case, increase in water vapour, through evaporation and/or moisture convergence, and vertical transport, leads to unstable environment, convective clouds development and precipitation. Maximum PWV at some locations is observed after peak precipitation, likely due to evaporative cold pools associated with precipitation. On small islands secondary peak in precipitation occurs during diurnal minimum of PWV, which indicates that interaction between clouds and radiation over surrounding oceans, or local seabreeze convergence are primary forcing mechanism.

4.3 Divergent diurnal behaviour between integrated moisture, cloud top temperature and precipitation

Most of stations across global tropics show consistent diurnal evolution of PWV, cloud top temperature and precipitation. A mono-modal diurnal cycle has been found to dominate diurnal evolution of atmospheric moisture at all stations. However, a number of locations exhibit significant semi-diurnal variability in precipitation and cloud top temperature. Here, an analysis of stations, that show no distinct diurnal variability, or show two noticeable extrema in precipitation or cloud top temperature, is provided.

Figure 5 shows diurnal evolution of PWV, precipitation and cloud top temperature at four locations characterized by differentiated diurnal evolution between those properties. All stations show relatively high daily mean PWV values exceeding 40 mm. REUN, NTUS and KOUR stations show a single peak in PWV during local afternoon, while COCO station shows virtually no distinct diurnal evolution in either integrated atmospheric moisture, precipitation or cloud top temperature. At the same time, REUN, NTUS and KOUR are characterized by rather clear diurnal evolution in cloud top temperature, for which a two minima occur throughout a day. The primary daily minimum Tb occurs during local afternoon (15–18 LT), while the second minimum is observed during early morning (3–5 LT). The nocturnal minimum is associated with higher Tb than during the primary one during the afternoon. It indicates that clouds' vertical extent is larger during the local afternoon than during night-time (e.g., deep convective thunderstorms vs congestus clouds). Precipitation also shows variability throughout a day across all stations. However, the magnitude of diurnal variability varies between 1 mm/day (Cocos Islands, Fig. 5a) and 15 mm/day (Singapore, Fig. 5c). All stations exhibit both diurnal and semi-diurnal modes, as manifested as two peaks in diurnal evolution (La Reunion, Singapore), a broad diurnal peak with two local maxima (French Guiana) or a modification to the 24-h cycle through an uptick in diurnal time series (Cocos Islands). Although there is a consistency between precipitation and cloud top temperature in the overall shape of diurnal evolution, the relative magnitudes of the two diurnal extrema as well as their phase differ between locations. At La Reunion, precipitation and cloud top temperature both show two extrema of comparable magnitude. The nocturnal extremum appears nearly in sync with PWV
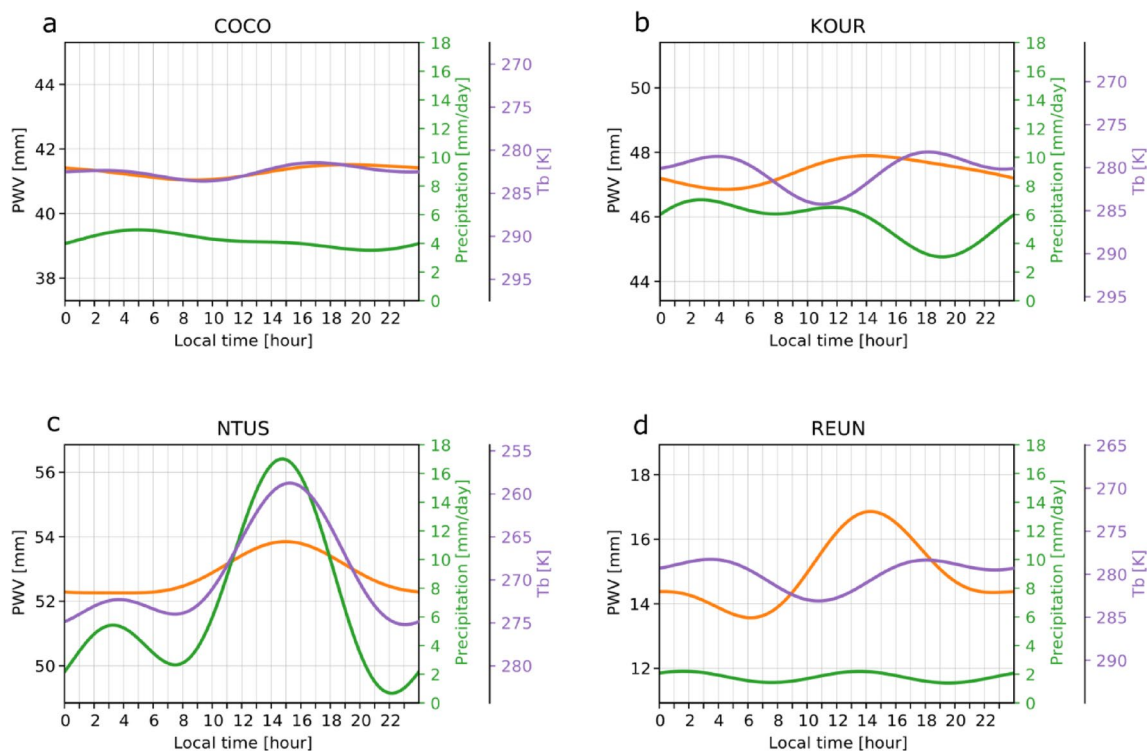
Fig. 5 Diurnal variations of PWV, Precipitation and IR data calculated for COCO (**a**), KOUR (**b**), NTUS (**c**), and REUN (**d**) stations based on entire time span

daily minimum, while the afternoon precipitation peak occurs during the daily maximum PWV and is followed by the daily minimum Tb. At Cocos Island, which is a small island as well, precipitation maxima occur in sync with Tb minima, while PWV remains at a nearly constant level. However, the night-time precipitation maximum is larger than the afternoon one, while cloud tops are colder during the afternoon peak in comparison with the nocturnal one. Thus, the nocturnal cloud population is shallower and produces more precipitation than deep convective clouds, which tend to occur during afternoon. Cocos Island is a small tropical island, and it is possible that precipitation associated with deep convective clouds occurs over water rather than over the atoll itself. Furthermore, observed variability in cloud top temperature and precipitation cannot be explained by modulation in moisture content within the atmospheric column. At Singapore location (Fig. 5c) the cloud top temperature and precipitation variability are well correlated. The maximum precipitation occurs during afternoon and is associated with daily lowest Tb value. The secondary peak in precipitation is nocturnal with magnitude of about 30% of the primarily afternoon peak. Associated Tb modulation is similarly smaller at that time. Therefore, deeper convective clouds are associated with strong afternoon precipitation, while shallower convective clouds are responsible for the secondary peak. The former occurs during daily maximum

PWV, while the latter is associated with daily minimum integrated atmospheric moisture. Over French Guiana (KOUR, Fig. 5b) precipitation is shifted towards the first half of a day. Maximum precipitation is observed around 3am, while the second, marginally smaller peak occurs around noon. The latter one is associated with the diurnal maximum in PWV. Cloud top temperature also shows bi-modal distribution, with one minimum during the early morning maximum in precipitation and the second in the afternoon (around 6 pm), which coincides with diurnal minimum in precipitation. The night-time precipitation maximum during diurnal minimum of atmospheric moisture content is consistent with dynamical forcing of convective clouds, likely due to convergence between northeasterly onshore flow and local sea-breeze circulation (Kousky 1980 MWR). Furthermore, morning to noon development of precipitation along the coastline is typical for diurnal in-land progression of convective cloud systems in the Amazon region, especially during boreal winter (Gerraud and Wallace 1997).

4.4 Insight into seasons

Previously presented results were based on analysis of the composite multi-year annual-mean diurnal cycle of humidity, precipitation and cloud top temperature, which by default removes any seasonal variations. To investigate

Table 1 Diurnal PWV amplitude at stations located on islands smaller than 550 km^2

Site	Location	Area (m^2)	Station height (m ASL)	Season			
				DJF (mm)	MAM (mm)	JJA (mm)	SON (mm)
ASPA	American Samoa	199	21.1	0.21	0.15	0.13	0.28
TUVA	Tuvalu	26	3.6	0.28	0.28	0.03	0.23
GUAM	Guam	544	146.4	0.10	0.09	0.23	0.19
TONG	Tonga (Tongatapu island)	257	3.7	0.37	0.31	0.18	0.29
CKIS	Cook Islands	236	5.7	0.29	0.19	0.25	0.27
DGAR	Diego Garcia	30	9.1	0.35	0.22	0.11	0.15
COCO	Coco Islands	24	3.4	0.29	0.23	0.17	0.28
CRO1	Vergin Islands	214	12.2	0.33	0.15	0.14	0.13
HNLC	Hawaii (Honolulu)	177.2	6.3	0.25	0.28	0.17	0.20

differences in the diurnal cycle of PWV in the context of seasons, for each of the stations we estimated the diurnal amplitude, phase and mean value with division into four seasons: December, January, February (DJF); March, April, May (MAM); June, July, August (JJA) and September, October, November (SON). Since general differences between PWV, Precipitation and TB data were already highlighted, here we focused exclusively on PWV to verify its response to the various weather patterns on a seasonal scale. Figure 7 presents obtained results. It is shown that stations located on the smallest islands generally exhibit a lack of significant diurnal cycle, regardless of the season. However, minor variations between DJF, MAM, JJA and SON were still found. In each case, the amplitude did not exceed 0.4 mm. This is summarized in Table 1, which provides detailed information for the stations with the smallest diurnal amplitude (below 0.4 mm) in all seasons. In this case two Hawaiian stations (MKEA and MAUI) are excluded as low values there are primarily due to high altitudes (above 3000 m ASL). A strong correlation between the ratio of daily and subdaily amplitude to mean PWV and the size of the land on which station is located is shown on the Fig. 6. Since the seasonal PWV variations for these stations are small, we present the relationship between the ratio of the daily and subdaily amplitude to the mean PWV value based on all available time span. Stations for which this ratio is below 1% for daily and 0.5% for subdaily signal (red square) are ASPA, COCO, CRO1, DGAR, GUAM, HNLC, PNGM, TONG and TUVA, all located on small islands at low altitudes (all pointed in Table 1, with the exception of PNGM station, but in this particular case the station is located at the peninsula of Manus Island—Lombrum province in Papua New Guinea). Such small islands without variated orography are exhibited to the oceanic weather patterns and therefore results obtained present typical oceanic weather conditions.

Although stations presented in Table 1 were in a very good agreement regarding small diurnal amplitude, they slightly varied in mean, seasonal PWV (Fig. 7, note that in the case of this figure, we present values of all amplitudes, including those smaller than 0.5 mm). Stations located in the northern hemisphere (GUAM, HNLC, CRO1) were characterised by higher PWV values during the JJA and SON, while stations located in the southern hemisphere (ASPA, TUVA, TONG, CKIS, DGAR, COCO) reached higher values during the DJF and MAM. This is a general feature that is not limited to small islands. In fact, seasonal changes in PWV characterise tropical and sub-tropical climates globally. For some stations, this variation directly reflects changes in the specific position of the Inter Tropical Convergence Zone (ITCZ), associated with elevated values of humidity and convective activity. In some areas, the differences are mainly caused by the Southeast Asian monsoon, which in JJA carries moisture towards Northern Hemisphere and in DJF towards Southern Hemisphere.
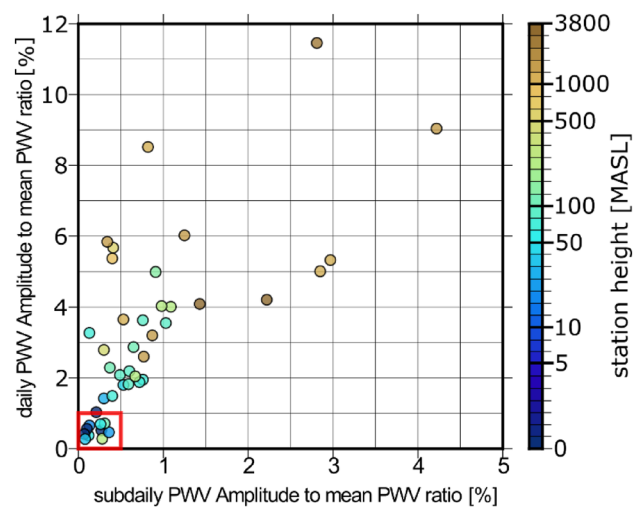
Fig. 6 Scatter of the ratio of daily PWV and subdaily PWV amplitude to the mean PWV value for each of analysed stations. The red square includes all stations from the Table 1

Fig. 7 Diurnal amplitude, phase and mean PWV for DJF, MAM, JJA and SON and each of analysed station
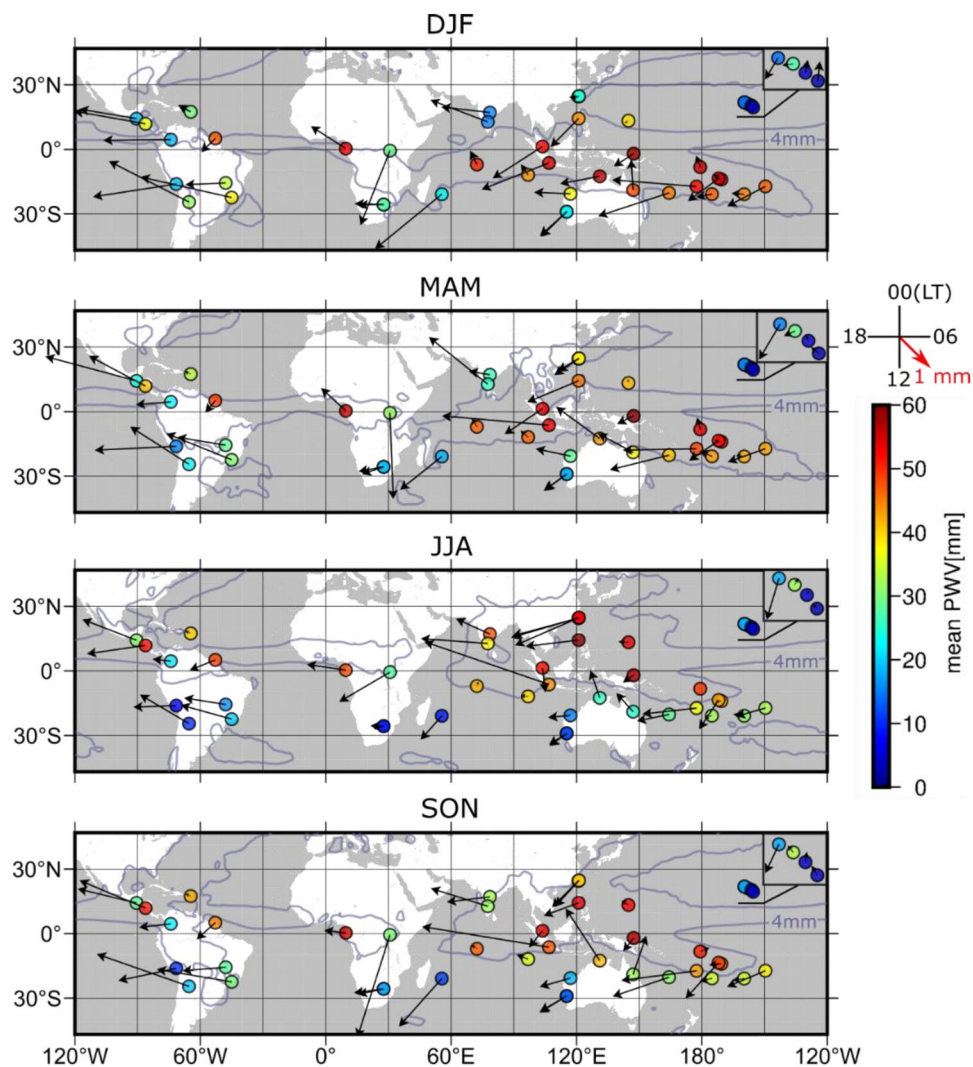
In fact, mean PWV in India obtained in JJA were three times (HYDE) or twice (IISC) as high as in DJF, while it was opposite in north Australian station located in Darwin (DARW). Interesting differences were also captured in northern Taiwan (TWTF, TNML, TCMS). Although this part of the island is characterized by rather high humidity throughout the whole year, there is a jump both in mean PWV and diurnal amplitude during boreal summer (JJA) compared to boreal winter (DJF). East Asian summer monsoon changes the large-scale flow regime over the area, which results in different weather systems affecting Taiwan and seasonal variations in PWV. During the summer monsoon season (May–September), deep cumulus convection frequently occurs over the region and quickly develops into organized convective storms. During midsummer, more than half of the rainfall is produced by diurnal convection along the western mountain slopes of the island (Wang and Chen 2008), which explains the jump in the diurnal amplitude of GPS-derived PWV.

5 Discussion and conclusion

In this paper, we analysed the coupling between moisture, clouds and precipitation in the tropical atmosphere based on long-term satellite records and coherent decomposition of time series data for 42 stations across global tropics. Due to a relationship between water vapour variability, convective process and precipitation (Neelin et al. 2009), PWV derived from the global navigation satellite system, rainfall estimates from TRMM (3B42 v 7 product), and cloud top temperature based on global merged infrared datasets were used to identify relations between the development of clouds and precipitation, and moisture variability across global tropics on a diurnal time scale.

Diurnal changes of integrated atmospheric moisture in the tropics are significantly smaller than the mean water vapour content in the atmosphere and rarely exceed 10%, which is consistent with other studies (Tian et al. 2004). However, it should be noted that in a favourable, conditionally unstable

atmosphere, even small changes to the stratification can lead to convection (Li and Carbone 2012). The daily mean values are primarily determined by station height and location in terms of the distance to the coast.

Similar results but oriented on the Sumatra region and much shorter data records, were shown by Torri et al. (2019). The PWV variability is characterized by mono-modal distribution with a single diurnal maximum during local afternoon, which is consistent with moistening through evaporation and convergence driven by solar radiation over land (Meza et al. 2020). Distinct diurnal evolution of the GNSS integrated moisture is also typical for the continental/large island areas. In contrast, small islands are characterized by relatively small changes in water vapour content on a subdiurnal time scale. The ratio of their amplitudes to mean values is 1.0% and 0.5% for daily and sub-daily amplitudes, respectively. This shows that GNSS-delivered diurnal variability of PWV is in line with other studies describing tropical diurnal cycle over land and ocean (Gray and Jacobson 1977; Yang and Slingo 2001; Nesbitt and Zipser 2003; Torri et al. 2019; Chepfer et al. 2019).

The afternoon maximum of the integrated atmospheric moisture is consistent with the occurrence of the precipitation maximum and cloud top temperature minimum at a majority of analysed locations. Also, afternoon decrease in cloud top temperature and development of convective precipitation tend to occur in response to diurnal increase in tropospheric moisture, especially on continental and large-islands stations. This confirms that afternoon precipitation is driven locally in a response to diurnal solar heating. However, favourable large-scale conditions are required for diurnal development of convection and precipitation. Over locations with strong subsidence (e.g., YARR, KARR) even substantial diurnal amplitude in tropospheric moisture content is not sufficient to destabilize atmosphere and initiate convection. A good proxy for mean large-scale conditions is given by the daily mean PWV—low values at stations located near sea level indicate overall dry, subsidence conditions with low chance for convection development on daily basis. Exceptions to this mechanism were only found at stations located on small islands [e.g., COCO (Cocos Island)], where significant diurnal variations in precipitation were observed, while PWV subdiurnal variability was only marginal. It is likely that over small islands local convergence driven by a boundary layer friction is more important than local moisture convergence. It should also be emphasized that beside the afternoon precipitation peak, several stations located on small islands were characterized by a second peak that appears during at night or during early morning hours, which is common in the oceanic climate regime (Chen and Houze 1997). This secondary precipitation peak occurred

during diurnal minimum of tropospheric moisture content variability, which showed a clear monomodal distribution at all stations. It was associated with decreased cloud top temperature and likely driven by advection of precipitating cloud systems from surrounding oceans.

The mono-modal diurnal distribution of the integrated moisture does not change with the seasons. Diurnal maximum occurs during local afternoon at all stations (except one located at 3000 m ASL). However, the average PWV values and its diurnal amplitude clearly reflect seasonality. Significantly higher PWV values characterize stations located in the northern (southern) hemisphere during JJA (DJF) compared to DJF (JJA). For some stations, the seasonal difference in the diurnal amplitude reflects changes in large-scale flow related to, e.g., Southeast Asian monsoon.

This study confirmed the usefulness of the GNSS technique for integrated atmospheric moisture variability studies and its applicability to an analysis of high temporal resolution variability across the global tropics. The length of time-series and temporal resolution of the dataset allowed a decomposition of integrated water vaport data into diurnal and semi-diurnal components, using the same approache as typically applied to precipitation and Tb datasets, and assessment of typical diurnal variability of the three different thermodynamic parameters, for various climate regimes and seasons.

Our paper highlighted high consistency between GNSS-derived PWV, TRMM precipitation, and IR cloud top temperature. GNSS can be successfully used in deep convection or heavy weather monitoring, both in near real-time and climatological applications. Apart from the fact that GNSS is a cost-effective and stuff-free technique for PWV acquisition, its remarkable potential lies in the high temporal resolution of collected data. In the case of this study, a 1-h time resolution of GNSS PWV data was used. However, GNSS offers much higher frequency, and already collected data allowed for more than 20-year time series analysis. Additionally, the number of GNSS permanent networks and stations is constantly growing. As an example, International GNSS Service currently consists of more than 500 globally distributed stations that collect data constantly. There are also number of regional networks such as Sumatran GPS Array (SuGAr) or NOAA CORS Network (NCN) that also provide GNSS observations thus enabling for analysis of spatio-temporal integrated moisture variability from sub-daily to interannual time scales.

Appendix

See Table 2 here.

Table 2 Name, location, and coordinates of IGS stations used in the study

Site	Location	Longitude [°]	Latitude [°]	Altitude [m]	Time-span	Data completeness (%)
AREQ	Arequipa, Peru	− 71.49	− 16.47	2449.1	01.2001–12.2018	91.6
ASPA	Pago Pago, United States	− 170.72	− 14.33	21.1	08.2001–12.2018	91.1
BAKO	Cibinong, Indonesia	106.85	− 6.49	139.8	01.2001–12.2018	91.4
BOGT	Bogota, Colombia	− 74.08	4.64	2553.9	05.2002–12.2018	95.0
BRAZ	Brasilia, Brazil	− 47.88	− 15.95	1118.6	01.2001–12.2018	93.9
CHPI	Cachoeira Paulista, Brazil	− 44.99	− 22.69	620.8	05.2003–12.2018	88.9
COCO	Cocos (Keeling) Island, Australia	96.83	− 12.19	3.4	01.2001–12.2018	96.9
CRO1	Christiansted, Virgin Islands, United States	− 64.58	17.76	12.2	01.2001–12.2018	94.3
DARW	Darwin, Australia	131.13	− 12.84	74.7	04.2001–12.2018	94.2
DGAR	Diego Garcia Island, United Kingdom	72.37	− 7.27	9.1	01.2001–12.2018	79.2
FALE	Faleolo, Samoa	− 172.00	− 13.83	9.7	01.2001–12.2017	76.2
GUAM	Dededo, Guam	144.87	13.59	146.4	01.2001–12.2018	96.1
GUAT	Guatemala City, Guatemala	− 90.52	14.59	1517.3	01.2001–12.2018	89.8
HARB	Pretoria, South Africa	27.71	− 25.89	1532.8	01.2001–12.2018	94.3
HNLC	Honolulu, United States	− 157.86	21.30	6.3	01.2001–12.2018	92.1
HRAO	Krugersdorp, South Africa	27.69	− 25.89	1388.9	01.2001–12.2018	95.0
HYDE	Hyderabad, India	78.55	17.42	441.7	10.2002–12.2018	86.4
IISC	Bangalore, India	77.6	13.0	843.7	01.2001–12.2018	87.3
KARR	Karratha, Australia	117.10	− 20.98	116.7	01.2001–12.2018	94.2
KOKB	Kokee Park, Waimea, United States	− 159.66	22.13	1150.5	01.2001–12.2018	96.4
KOUC	Koumac, New Caledonia	164.29	− 20.56	23.7	01.2001–12.2018	88.1
KOUR	Kourou, French Guiana	− 52.81	5.25	8.7	01.2001–12.2018	90.0
LAUT	Lautoka, Fiji	177.45	− 17.61	31.7	12.2001–12.2018	88.8
MANA	Managua, Nicaragua	− 86.25	12.15	66.4	01.2001–12.2018	88.9
MAUI	Haleakala, Maui, United States	− 156.26	20.71	3044.1	01.2001–12.2018	92.1
MBAR	Mbarara, Uganda	30.74	− 0.60	1349.6	07.2001–12.2018	67.7
MKEA	Mauna Kea, United States	− 155.46	19.80	3728.4	01.2001–12.2018	95.8
NKLG	Libreville, Gabon	9.67	0.35	21.5	01.2001–12.2018	93.2
NTUS	Singapore, Singapore	103.68	1.35	71.6	02.2001–12.2018	76.2
PIMO	Quezon City, Philippines	121.08	14.64	51.4	04.2001–12.2018	88.9
PNGM	Lombrum, Papua New Guinea	147.37	− 2.04	38.7	05.2002–12.2018	85.7
REUN	Le Tampon, France	55.57	− 21.21	1552.2	01.2001–12.2018	87.2
TCMS	Hsinchu, Taiwan	120.99	24.80	58.4	08.2002–12.2018	81.6
THTI	Papeete, French Polynesia	− 149.61	− 17.58	90.8	01.2001–12.2018	95.5
TNML	Hsinchu, Taiwan	120.99	24.80	57.0	06.2002–12.2018	76.9
TONG	Nuku'alofa, Tonga	− 175.18	− 21.14	3.7	02.2002–12.2018	83.4
TOW2	Cape Ferguson, Australia	147.06	− 19.27	30.3	01.2001–12.2018	97.0
TUVA	Funafuti, Tuvalu	179.20	− 8.53	3.6	05.2002–12.2018	80.8
TWTF	Taoyuan, Taiwan	121.16	24.95	184.1	11.2001–12.2018	93.4
UNSA	Salta, Argentina	− 65.41	− 24.73	1224.4	01.2001–12.2018	88.1
YAR2	Yarragadee, Australia	115.35	− 29.05	267.0	01.2001–12.2018	96.5
YARR	Yarragadee, Australia	115.35	− 29.05	267.1	02.2001–12.2018	78.1

Availability of data and materials The hourly GNSS PWV data are available under the CC BY-NC-ND licence (Nykiel et al. 2023).

Declarations

Conflict of interest Authors have no competing interests as defined by Springer, or other interests that might be perceived to influence the results and/or discussion reported in this paper.

Ethical approval Not applicable.

References

Adams DK, Gutman SI, Holub KL, Pereira DS (2013) GNSS observations of deep convective time scales in the Amazon. Geophys Res Lett 40:2818–2823. https://doi.org/10.1002/grl.50573

Albright MD, Recker ER, Reed RJ, Dang R (1985) The diurnal variation of deep convection and inferred precipitation in the central tropical Pacific during January–February 1979. Mon Weather Rev 113:1663–1680. https://doi.org/10.1175/1520-0493(1985)113%3c1663:TDVODC%3e2.0.CO;2

Alvares CA, Stape JL, Sentelhas PC, de Moraes Gonçalves JL, Sparovek G (2013) Köppen's climate classification map for Brazil. Meteorol Z 22:711–728. https://doi.org/10.1127/0941-2948/2013/0507

Bain CL, Magnusdottir G, Smyth P, Stern H (2010) Diurnal cycle of the intertropical convergence zone in the east Pacific. J Geophys Res 115:D23116. https://doi.org/10.1029/2010JD014835

BakamaNume BB (2010) A contemporary geography of Uganda. African Books Collective, Der es Salaam

Baldysz Z, Nykiel G, Figurski M, Araszkiewicz A (2018) Assessment of the impact of GNSS processing strategies on the long-term parameters of 20 years IWV time series. Remote Sens 10(4):496. https://doi.org/10.3390/rs10040496

Baldysz Z, Nykiel G, Latos B, Baranowski DB, Figurski M (2021) Interannual variability of the GNSS precipitable water vapor in the global tropics. Atmosphere 12(12):1698. https://doi.org/10.3390/atmos12121698

Baranowski DB, Flatau MK, Flatau PJ, Matthews AJ (2016) Phase locking between atmospheric convectively coupled equatorial Kelvin waves and the diurnal cycle of precipitation over the Maritime Continent. Geophys Res Lett 43:8269–8276. https://doi.org/10.1002/2016GL069602

Baranowski DB, Waliser DE, Jiang X, Ridout JA, Flatau MK (2019) Contemporary GCM fidelity in representing the diurnal cycle of precipitation over the Maritime Continent. J Geophys Res Atmos 124:747–769. https://doi.org/10.1029/2018JD029474

Barindelli S, Realini E, Venuti G, Fermi A, Gatti A (2018) Detection of water vapor time variations associated with heavy rain in northern Italy by geodetic and low-cost GNSS receivers. Earth Planets Sp 70:28. https://doi.org/10.1186/s40623-018-0795-7

Bellenger H, Takayabu YN, Ushiyama T, Yoneyama K (2010) Role of diurnal warm layers in the diurnal cycle of convection over the tropical Indian Ocean during MISMO. Mon Weather Rev 138:2426–2433. https://doi.org/10.1175/2010MWR3249.1

Benevides P, Catalao J, Miranda P (2015) On the inclusion of GPS precipitable water vapour in the nowcasting of rainfall. Nat Hazards Earth Syst Sci 15:2605–2616. https://doi.org/10.5194/nhess-15-2605-2015

Bevis M, Businger S, Herring T, Rocken C, Anthes R, Ware R (1992) GPS meteorology: Remote sensing of atmospheric water vapor using the global positioning system. J Geophys Res 97:15787–15801. https://doi.org/10.1029/92JD01517

Bevis M, Businger S, Chiswell S, Herring T, Anthes R, Rocken C, Ware R (1994) GPS meteorology: mapping zenith wet delays onto precipitable water. J Appl Meteorol Climatol 33:379–386. https://doi.org/10.1175/1520-0450(1994)033%3c0379:GMMZWD%3e2.0.CO;2

Biasutti M, Yuter SE, Burleyson CD, Sobel AH (2012) Very high resolution rainfall patterns measured by TRMM precipitation radar: seasonal and diurnal cycles. Clim Dyn 39:239–258. https://doi.org/10.1007/s00382-011-1146-6

Boehm J, Werl B, Schuh H (2006) Troposphere mapping functions for GPS and very long baseline interferometry from European Centre for Medium-Range Weather Forecasts operational analysis data. J Geophys Res 111:B02406. https://doi.org/10.1029/2005JB003629

Bonner W (1968) Climatology of the low level jet. Mon Weather Rev 96:833–849. https://doi.org/10.1175/1520-0493(1968)096%3c0833:COTLLJ%3e2.0.CO;2

Bosser P, Bock O, Flamant C, Bony S, Speich S (2021) Integrated water vapour content retrievals from ship-borne GNSS receivers during EUREC4A. Earth Syst Sci Data 13:1499–1517. https://doi.org/10.5194/essd-13-1499-2021

Bowman KP, Fowler MD (2015) The diurnal cycle of precipitation in tropical cyclones. J Climate 28:5325–5334. https://doi.org/10.1175/JCLI-D-14-00804.1

Bowman KP, Collier JC, North GR, Wu Q, Ha E, Hardin J (2005) Diurnal cycle of tropical precipitation in Tropical Rainfall Measuring Mission (TRMM) satellite and ocean buoy rain gauge data. J Geophys Res 110:D21104. https://doi.org/10.1029/2005JD005763

Chen SS, Houze RA Jr (1997) Diurnal variation and lifecycle of deep convective systems over the tropical Pacific warm pool. Q J R Meteor Soc 123:357–388. https://doi.org/10.1002/qj.49712353806

Chepfer H, Brogniez H, Noel V (2019) Diurnal variations of cloud and relative humidity profiles across the tropics. Sci Rep 9:16045. https://doi.org/10.1038/s41598-019-52437-6

Ciesielski PE, Johnson RH, Schubert WH, Ruppert JH Jr (2018) Diurnal cycle of the ITCZ in DYNAMO. J Clim 31:4543–4562. https://doi.org/10.1175/JCLI-D-17-0670.1

Dach R, Lutz S, Walser P, Fridez P (2015) Bernese GNSS Software Version 5.2; User Manual. Astronomical Institute, University of Bern, Bern

Dai A (2001) Global precipitation and thunderstorm frequencies. Part I: seasonal and interannual variations. J Clim 14(6):1092–1111. https://doi.org/10.1175/1520-0442(2001)014<1092:GPATFP>2.0.CO;2

Dai A, Wigley TML, Boville BA, Kiehl JT, Buja LE (2001) Climates of the twentieth and twenty-first centuries simulated by the NCAR climate system model. J Clim 14:485–519. https://doi.org/10.1175/1520-0442(2001)014%3c0485:COTTAT%3e2.0.CO;2

Ding J, Chen J, Tang W, Song Z (2022) Spatial-temporal variability of global GNSS-derived precipitable water vapor (1994–2020) and climate implications. Remote Sens 14:3493. https://doi.org/10.3390/rs14143493

Garreaud RD, Wallace JM (1997) The diurnal march of convective cloudiness over the Americas. Mon Weather Rev 125:3157–3171. https://doi.org/10.1175/1520-0493(1997)125%3c3157:TDMOCC%3e2.0.CO;2

Gradinarsky LP, Johansson JM, Bouma HR, Scherneck HG, Elgered G (2002) Climate monitoring using GPS. Phys Chem Earth 27:335–340. https://doi.org/10.1016/S1474-7065(02)00009-8

Gray WM, Jacobson RW Jr (1977) Diurnal variation of deep cumulus convection. Mon Weather Rev 105:1171–1188. https://doi.org/10.1175/1520-0493(1977)105%3c1171:DVODCC%3e2.0.CO;2

Guerova G, Jones J, Dousa J, Dick G, de Haan S, Pottiaux E, Bock O, Pacione R, Elgered G, Vedel H, Bender M (2016) Review of the state of the art and future prospects of the ground-based GNSS meteorology in Europe. Atmos Meas Tech 9:5385–5406. https://doi.org/10.5194/amt-9-5385-2016

Guerova G, Douša J, Dimitrova T, Stoycheva A, Václavovic P, Penov N (2022) GNSS storm nowcasting demonstrator for Bulgaria. Remote Sens 14:3746. https://doi.org/10.3390/rs14153746

Hassim MEE, Lane TP, Grabowski WW (2016) The diurnal cycle of rainfall over New Guinea in convection-permitting WRF simulations. Atmos Chem Phys 16:161–175. https://doi.org/10.5194/acp-16-161-2016,2016

Herring TA (1992) Modeling atmospheric delays in the analysis of space geodetic data. In: De Munck JC, Spoelstra TA (eds) Proceedings of the refraction of transatmospheric signals in geodesy, Geodetic Commission Publications on Geodesy, Netherlands

Hersbach H, Bell B, Berrisford P et al (2020) The ERA5 global reanalysis. Q J R Meteorol Soc 146:1999–2049. https://doi.org/10.1002/qj.3803

Hou AY, Kakar RK, Neeck S, Azarbarzin AA, Kummerow CD, Kojima M, Oki R, Nakamura K, Iguchi T (2014) The global precipitation measurement mission. Bull Am Meteorol Soc 95:701–722. https://doi.org/10.1175/BAMS-D-13-00164.1

Huffman GJ, Adler RF, Bolvin DT, Nelkin EJ (2010) The TRMM multi-satellite precipitation analysis (TMPA). In: Gebremichael M, Hossain F (eds) Satellite rainfall applications for surface hydrology. Springer, Dordrecht. https://doi.org/10.1007/978-90-481-2915-7_1

Janowiak JE, Arkin PA, Morrissey M (1994) An examination of the diurnal cycle in oceanic tropical rainfall using satellite and in situ data. Mon Weather Rev 122:2296–2311. https://doi.org/10.1175/1520-0493(1994)122%3c2296:AEOTDC%3e2.0.CO;2

Janowiak JE, Joyce RJ, Yarosh Y (2001) A real-time global half-hourly pixel-resolution infrared dataset and its applications. Bull Am Meteorol Soc 82:205–218. https://doi.org/10.1175/1520-0477(2001)082%3c0205:ARTGHH%3e2.3.CO;2

Johnson RH, Rickenbach TM, Rutledge SA, Ciesielski PE, Schubert WH (1999) Trimodal characteristics of tropical convection. J Clim 12:2397–2418. https://doi.org/10.1175/1520-0442(1999)012%3c2397:TCOTC%3e2.0.CO;2

Jones J, Guerova G, Douša J, Dick G, de Haan S, Pottiaux E, Bock O, Pacione R, van Malderen R (eds) (2020) Advanced GNSS tropospheric products for monitoring severe weather events and climate. Springer, Cham. https://doi.org/10.1007/978-3-030-13901-8

Kikuchi K, Wang B (2008) Diurnal precipitation regimes in the global tropics. J Clim 21:2680–2696. https://doi.org/10.1175/2007JCLI2051.1

Kirkland EJ (2010) Bilinear interpolation. Advanced computing in electron microscopy. Springer, Boston. https://doi.org/10.1007/978-1-4419-6533-2_12

Köppen W (1936) Das geographische system der klimat. Handbuch der klimatologie. Berlin

Kottek M, Grieser J, Beck C, Rudolf B, Rubel F (2006) World Map of the Köppen-Geiger climate classification updated. Meteorol Z 15:259–263. https://doi.org/10.1127/0941-2948/2006/0130

Kousky V (1980) Diurnal rainfall variations in northeast Brazil. Mon Weather Rev 108:488–498. https://doi.org/10.1175/1520-0493(1980)108%3c0488:DRVINB%3e2.0.CO;2

Li Y, Carbone RE (2012) Excitation of rainfall over the tropical western pacific. J Atmos Sci 69:2983–2994. https://doi.org/10.1175/JAS-D-11-0245.1

Li G, Kimura F, Sato T, Huang D (2008) A composite analysis of diurnal cycle of GPS precipitable water vapor in central Japan during Calm Summer Days. Theor Appl Climatol 92:15–29. https://doi.org/10.1007/s00704-006-0293-x

Liu C, Zipser EJ (2008) Diurnal cycles of precipitation, clouds, and lightning in the tropics from 9 years of TRMM observations. Geophys Res Lett 35:L04819. https://doi.org/10.1029/2007GL032437

Mapes BE, Houze RA Jr (1993) Cloud clusters and superclusters over the oceanic warm pool. Mon Weather Rev 121:1398–1416. https://doi.org/10.1175/1520-0493(1993)121%3c1398:CCASOT%3e2.0.CO;2

Marzuki M, Suryanti K, Yusnaini H, Tangang F, Muharsyah R, Vonnisa M, Devianto D (2021) Diurnal variation of precipitation from the perspectives of precipitation amount, intensity and duration over Sumatra from rain gauge observations. Int J Climatol 41:4386–4397. https://doi.org/10.1002/joc.7078

Matthews AJ (2012) A multiscale framework for the origin and variability of the South Pacific Convergence Zone. Q J R Meteorol Soc 138:1165–1178. https://doi.org/10.1002/qj.1870

McGarry MM, Reed RJ (1978) Diurnal variations in convective activity and precipitation during phases II and III of GATE. Mon Weather Rev 106:101–113. https://doi.org/10.1175/1520-0493(1978)106%3c0101:DVICAA%3e2.0.CO;2

Meza A, Mendoza L, Natali MP, Bianchi C, Fernández L (2020) Diurnal variation of precipitable water vapor over Central and South America. Geod Geodyn 11:426–441. https://doi.org/10.1016/j.geog.2020.04.005

Neelin JD, Peters O, Hales K (2009) The transition to strong convection. J Atmos Sci 66:2367–2384. https://doi.org/10.1175/2009JAS2962.1

Nesbitt SW, Zipser EJ (2003) The diurnal cycle of rainfall and convective intensity according to three years of TRMM measurements. J Clim 16:1456–1475. https://doi.org/10.1175/1520-0442(2003)016%3c1456:TDCORA%3e2.0.CO;2

Nicholls ME (2015) An investigation of how radiation may cause accelerated rates of tropical cyclogenesis and diurnal cycles of convective activity. Atmos Chem Phys 15:9003–9029. https://doi.org/10.5194/acp-15-9003-2015

Nykiel G, Figurski M, Baldysz Z (2019) Analysis of GNSS sensed precipitable water vapour and tropospheric gradients during the derecho event in Poland of 11th August 2017. J Atmos Sol. https://doi.org/10.1016/j.jastp.2019.105082

Nykiel G, Figurski M, Bałdysz Z (2023) Hourly GNSS-derived integrated moisture in the global tropics for the years 2001–2018. Gdańsk Univ Technol. https://doi.org/10.34808/7nf0-h589

Ortiz de Galisteo JP, Cachorro V, Toledano C, Torres B, Laulainen N, Bennouna Y, de Frutos A (2011) Diurnal cycle of precipitable water vapor over Spain. Q J R Meteorol Soc 137:948–958. https://doi.org/10.1002/qj.811

Parracho AC, Bock O, Bastin S (2018) Global IWV trends and variability in atmospheric reanalyses and GPS observations. Atmos Chem Phys 18:16213–16237. https://doi.org/10.5194/acp-18-16213-2018

Ramage CS (1964) Diurnal variation of summer rainfall of Malaysia. J Trop Geogr 19:62–68

Ray CL (1928) Diurnal variation of rainfall at San Juan, P.R. Mon Weather Rev 56:140–141. https://doi.org/10.1175/1520-0493(1928)56%3c140:DVORAS%3e2.0.CO;2

Roth M (2007) Review of urban climate research in (sub)tropical regions. Int J Climatol 27:1859–1873. https://doi.org/10.1002/joc.1591

Rüger JM (2002) Refractive index formulae for radio waves. In: Proceedings of the FIG XXII international congress, Washington, D.C., USA

Ruppert JH, Johnson RH (2015) Diurnally modulated cumulus moistening in the pre-onset stage of the Madden-Julian Oscillation during DYNAMO. J Atmos Sci 72:1622–1647. https://doi.org/10.1175/JAS-D-14-0218.1

Rupert JH, Johnson RH (2016) On the cumulus diurnal cycle over the tropical warm pool. J Adv Model Earth Syst 8:669–690. https://doi.org/10.1002/2015MS000610

Saastamoinen J (1972) Atmospheric correction for the troposphere and stratosphere in ranging satellites. In: Henriksen SW, Mancini A, Chovitz BH (eds) The use of artificial satellites for geodesy. American Geophysical Union, Washington, DC. https://doi.org/10.1029/GM015p0247

Sakaeda N, Kiladis G, Dias J (2020) The diurnal cycle of rainfall and the convectively coupled equatorial waves over the maritime continent. J Clim 33:3307–3331. https://doi.org/10.1175/JCLI-D-19-0043.1

Salgado AAR, Assis WL, Magalhães Júnior AP, do Carmo FF, de Sordi MV, de Oliveira FS, (2019) Semi-humid: the landscape of Central Brazil. The physical geography of Brazil. Springer, Cham. https://doi.org/10.1007/978-3-030-04333-9

Seidel D, Sun B, Pettey M, Reale A (2011) Global radiosonde balloon drift statistics. J Geophys Res 116:D07102. https://doi.org/10.1029/2010JD014891

Serra YL, McPhaden MJ (2004) In situ observations of diurnal variability in rainfall over the tropical Pacific and Atlantic oceans. J Clim 17:3496–3509. https://doi.org/10.1175/1520-0442(2004)017%3c3496:ISOODV%3e2.0.CO;2

Serrano-Vincenti S, Condom T, Campozano L, Escobar LA, Walpersdorf A, Carchipulla-Morales D, Villacís M (2022) Harmonic analysis of the relationship between GNSS precipitable water vapor and heavy rainfall over the Northwest Equatorial Coast, Andes, and Amazon Regions. Atmosphere 13:1809. https://doi.org/10.3390/atmos13111809

Simpson J, Kummerow C, Tao WK, Adler RF (1996) On the tropical rainfall measuring mission (TRMM). Meteor Atmos Phys 60:19–36. https://doi.org/10.1007/BF01029783

Smith GL, Rutan DA (2003) The diurnal cycle of outgoing longwave radiation from Earth Radiation Budget Experiment measurements. J Atmos Sci 60:1529–1542. https://doi.org/10.1175/2997.1

Steigenberger P, Lutz S, Dach R, Schaer S, Jäggi A (2016) CODE Repro2 Product Series for the IGS. Astronomical Institute, University of Bern, Bern

Suparta W, Ali M (2014) Nowcasting the lightning activity in Peninsular Malaysia using the GPS PWV during the 2009 inter-monsoons. Ann Geophys. https://doi.org/10.4401/ag-6373

Takayabu YN (2002) Spectral representation of rain profiles and diurnal variations observed with TRMM PR over the equatorial area. Geophys Res Lett 29:1584. https://doi.org/10.1029/2001GL014113

Tian B, Soden BJ, Wu X (2004) Diurnal cycle of convection, clouds, and water vapor in the tropical upper troposphere: satellites versus a general circulation model. J Geophys Res 109:D10101. https://doi.org/10.1029/2003JD004117

Torri G, Adams DK, Wang H, Kuang Z (2019) On the diurnal cycle of GPS-derived precipitable water vapor over Sumatra. J Atmos Sci 76:3529–3552. https://doi.org/10.1175/JAS-D-19-0094.1

Vaquero-Martinez J, Anton M (2021) Review on the role of GNSS meteorology in monitoring water vapor for atmospheric physics. Remote Sens 13:2287. https://doi.org/10.3390/rs13122287

Wallace JM (1975) Diurnal variations in precipitation and thunderstorm frequency over the conterminous United States. Mon Weather Rev 103:406–419. https://doi.org/10.1175/1520-0493(1975)103%3c0406:DVIPAT%3e2.0.CO;2

Wang S, Chen T (2008) Measuring East Asian summer monsoon rainfall contributions by different weather systems over Taiwan. J Appl Meteor Climatol 47:2068–2080. https://doi.org/10.1175/2007JAMC1821.1

Wu Q, Ruan Z (2016) Diurnal variations of the areas and temperatures in tropical cyclone clouds. Q J R Meteorol Soc 142:2788–2796. https://doi.org/10.1002/qj.2868

Yang GY, Slingo J (2001) The diurnal cycle in the tropics. Mon Weather Rev 129:784–801

Yang S, Kuo KS, Smith EA (2008) Persistent nature of secondary diurnal modes of precipitation over oceanic and continental regimes. J Clim 21:4115–4131. https://doi.org/10.1175/2008JCLI2140.1

Zhao Q, Yao Y, Yao W (2018) GPS-based PWV for precipitation forecasting and its application to a typhoon event. J Atmos Sol 167:124–133. https://doi.org/10.1016/j.jastp.2017.11.013

Publisher's Note Springer Nature remains neutral with regard to jurisdictional claims in published maps and institutional affiliations.